Nonadiabatic Study of Dynamic Electronic Effects during Brittle Fracture of Silicon

Patrick L. Theofanis, Andres Jaramillo-Botero,* William A. Goddard III,† and Hai Xiao

Division of Chemistry and Chemical Engineering, California Institute of Technology,
1200 East California Boulevard, Pasadena, California 91125, USA

It has long been observed that brittle fracture of materials can lead to emission of high energy electrons and UV photons, but an atomistic description of the origin of such processes has lacked. We report here on simulations using a first-principles-based electron force field methodology with effective core potentials to describe the nonadiabatic quantum dynamics during brittle fracture in silicon crystal. Our simulations replicate the correct response of the crack tip velocity to the threshold critical energy release rate, a feat that is inaccessible to quantum mechanics methods or conventional force-field-based molecular dynamics. We also describe the crack induced voltages, current bursts, and charge carrier production observed experimentally during fracture but not previously captured in simulations. We find that strain-induced surface rearrangements and local heating cause ionization of electrons at the fracture surfaces.

PACS numbers: 62.20.mj, 31.15.xg, 46.50.+a

The observation that brittle fracture of materials can lead to the emission of high energy electrons and UV photons is well documented for materials ranging from polymer thermoplastics, glasses, minerals, and semiconductor crystals [1–4]. There has been no previous atomistic description of the origin of such processes. Although fracture in solids involves breaking of chemical bonds, which can be well described with modern quantum mechanics (QM) methods, the observation of exoelectrons and photon emissions indicates that the processes are not purely adiabatic, complicating the application of QM—in particular for model systems that require more than a few hundred atoms. We show here that the recently developed first-principles-based electron force field (eFF) method for nonadiabatic dynamics accounts for electron emission and large potential differences consistent with the experiments, providing the first atomistic description of the origin of these effects. In this Letter we consider the fracture of silicon crystals producing {100} and {111} fracture planes which have been studied quite thoroughly. The effects that we explain are (1) loading of a crack leads to a sudden onset of crack propagation at 7 GPa followed by uniform velocity of the crack at 2500 km/ sec after initiation and (2) voltage fluctuations in the 10–400 mV range, charge creation (up to 10^{11} carriers/cm^2), and current production (up to 1.3 mA).

It was not possible to explain the sudden onset of crack propagation and constant velocity response to increasing loads observed in the brittle fracture of silicon with earlier force-fields-based methods (e.g., Tersoff, Stillinger-Weber) [5–8]. However, Buehler and co-workers demonstrated that the reactive force file, ReaxFF, correctly describes the experimentally observed crack dynamics in silicon [9–11]. Left unexplained, however, is the generation of voltages and currents during fracture [12,13]. More recent experimental studies have observed the ejection of electrons [14] and other charged particles [15] during

silicon fracture dynamics. No previous attempts were made to model the voltage fluctuations, electron emission, and charge creation phenomena. Current time-dependent QM methods are incapable of describing the dynamics of electron ejection excitation of highly excited states from deformation of the crystal. Quantum mechanical methods are unable to attain the length and time scales (> 1000 atoms over >1 ps time scales) required to describe the dynamics of fracture. On the other hand, conventional force fields in conjunction with molecular dynamics methods can handle the relevant length and time scales, but they do not describe ejected electrons and excited electronics states. The eFF method allows us to capture the appropriate length and time scales, and most importantly, the electron dynamics during fracture.

The eFF method provides an approximate description of quantum dynamics by describing every electron as a floating spherical Gaussian orbital [16] whose position and size varies dynamically while the nuclei are treated as classical point charge particles. Here the total N-electron wave function is written as a Hartree product of one-electron orbitals (rather than as an antisymmetrized product). Orthogonality resulting from the Pauli principle is enforced with a spin-dependent Pauli repulsion Hamiltonian which is a function of the sizes and separations of these Gaussian orbitals. The Pauli potential accounts for the kinetic energy change due to orthogonalization, arising from the Pauli principle (antisymmetrization) [17,18]. An additional quantum-derived term in the eFF Hamiltonian is the kinetic energy for each orbital, which accounts for the Heisenberg principle. The full Hamiltonian in eFF also incorporates classical electrostatic terms between nuclei or electrons. eFF has been validated on challenging electronic phenomena arising in materials subjected to extreme conditions including Auger processes [19], hypervelocity impact, and plasma formation [20].

Previously eFF treated all electrons of an atom, including the core electrons [21]. Describing the very short time scales of the high energy core orbitals makes simulating picoseconds of fracture computationally intractable on systems large enough to describe crack propagation in Si crystal. Instead of describing all electrons explicitly, here we replace the core electrons with an effective core pseudopotential while retaining the accuracy in describing the valence electrons. This allows us to study the dynamics of electronic excitations and ejection simultaneous with nucleation and propagation of crack fracture in silicon. This approximation is described in detail in the Supplemental Material [22].

For this study we developed two simulation cells. Figure 1 depicts our "{100}" crack model. In this model the x-y-z directions are $(100) \times (011) \times (01\bar{1})$ direction, creating a (100) fracture plane with a [011] fracture direction with dimensions of $3.8 \times 25 \times 3.8$ nm^3. In our "{111}" model, the x-y-z directions are $(111) \times (\frac{\bar{1}}{2}\frac{\bar{1}}{2}\bar{1}) \times (\frac{1}{2}\frac{\bar{1}}{2}0)$ which produces 111 crack surfaces with a [112] crack propagation direction with dimensions of $2.7 \times 47 \times 4.0$ nm^3. We performed crack simulations on fully periodic replicas and on slabs with hydrogen-passivated surfaces of the previously described geometries. The results presented here correspond to our fully periodic system, though we found negligible differences between the results we obtain in our fully periodic and partially periodic slab models (see Fig. 2). Both systems were prepared in an isothermal-isobaric ensemble using a Nosé-Hoover thermostat and barostat, at 300 K and 1 atm, respectively. In both samples a seed crack of length $\frac{1}{5}L_y$ is created before a load is applied. A continuous uniaxial strain load is applied to
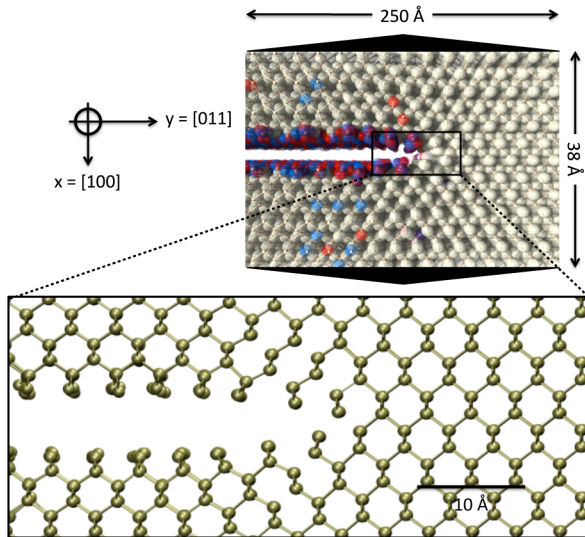
the cells in the x dimension at a rate of 1.2% per ps and the sample is allowed to crack naturally, which allows us to test the failure modes of the system. No barostat pressure is imposed in the strain direction.

Figure 2 shows the relationship between the crack tip velocity and the energy release rate normalized by the critical energy release rate determined at the onset of fracture. We computed G from the uniaxial stress ahead of the crack, the crack length, and Young's modulus that we compute from our model: $G = 1.12^2 \pi P_{xx}^2 a / E^2$. K_{ic} is computed similarly. Both the {100} and {111} models exhibit brittle fracture and both match the experimental observation that upon reaching a critical load, the crack velocity rapidly jumps to 4 and 2 km/s, respectively, and plateaus thereafter (data for the eFF {100} model are in the Supplemental Material [22]). Table I compares computed mechanical properties to those of experiments. The calculated Griffith critical load for the {111} is 3.16 J/m^2, which is higher than the experimental value but in agreement with the QM value of 3.1 J/m^2 [29]. This indicates that our model leads to a small amount of lattice trapping. In general, our simulations of the dynamics of fracture in silicon using the eFF pseudopotential reproduce experimental measurements and results produced with other reactive force fields [10].

From our simulations we ascertain that there are two prevalent modes of electron ionization: local field-induced ionization and thermal ionization. The simulations show that ionization occurs as a direct result of fracture. Figure 3 shows the evolution of a representative group of electrons as the fracture progresses. We find that electron ionization is precipitated by the passing of the crack front. Figure 3(c) shows that ionized electrons are excited by 5 eV, making
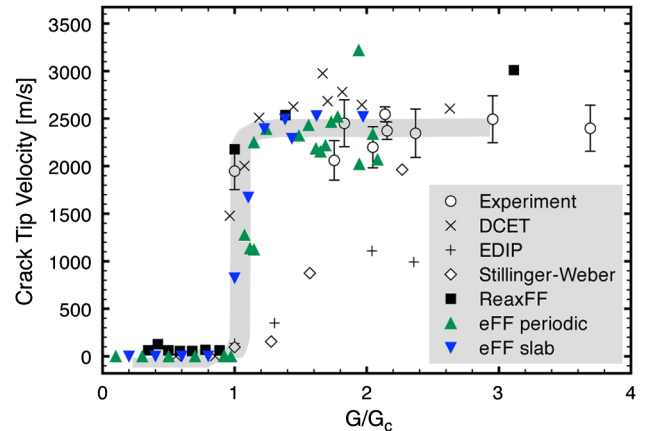

FIG. 1 (color online). A snapshot of a crack propagating in a silicon single crystal with mode I loading in the x direction producing a {100}⟨011⟩ edge crack. The transparent spheres are paired electrons. Unpaired spin-up and spin-down electrons are shaded.

FIG. 2 (color online). Crack tip velocity versus reduced load for {111} fracture with experimental data from [5], ReaxFF-Tersoff and Stillinger-Weber data from [10], environmental dependent interatomic potential (EDIP) and the results of a multiscale method that couples empirical potentials and quantum mechanical tight-binding approaches (DCET) from [31]. The gray line is a visual guide.

TABLE I.   Comparison of experimental and computed mechanical values: Young's modulus E (GPa), yield strength (GPa), Griffith critical load G_c (J/m^2), and the stress intensity factor K_{ic} (MPa). References are in square brackets.

Method	E	Yield strength	G_c	K_{ic}
{111} expt.	163–188 [23]	7 [24]	2.3 [5]	0.76 [25,26]
{111} eFF	166	15	3.16	0.752
{100} expt.	125–202 [27]	$\cdots$	$\cdots$	0.91 [28]
{100} eFF	157	15	2.57	0.96

them sufficiently energetic to escape the Si-surface barrier. The initial excitation promotes the electrons to unbound states (total electron energy >0), but they subsequently relax to 4.1 eV above the ground state, well into the Si conduction band. A close examination of the energy contributions leading to ionization reveals that in most cases an increase in potential energy causes ionization. The cause of this is heterolytic bond cleavage across the crack. In rare instances a heterolytic cleavage creates an anion on one crack face and a cation on the other crack face. As dangling bonds form 2×1 surface dimers, the excess electron causes Pauli exclusion clashes with adjacent surface pairs. As a result, the ionized electron's radius decreases to reduce its overlap with nearby same-spin electrons. The spin clashing forces the electron further from the surface and the electron delocalizes (its radius increases in the eFF description). Ultimately it relaxes and settles into the conduction band. $80 \pm 10\%$ of ionized electrons are ionized because of local field effects.

In rare circumstances an increase in an electron's kinetic energy after fracture causes it to ionize. Kinetic excitation is caused by local heating so we conclude that while possible, thermal ionization is not the predominant mechanism. In Fig. 2 of the Supplemental Material [22] the kinetic energy of the same group of electrons depicted in Fig. 3 are presented. In that figure only one electron is excited thermally—the fingerprint of thermal excitation in increased kinetic energy. We observe that elastic energy in the stress field ahead of the crack is converted to kinetic energy in the recoil of the new surfaces causing local heating. As mentioned previously, we estimate that $20 \pm 10\%$ of the electrons are thermally ionized.

To understand the dynamics of charge carriers during silicon fracture, we compute the electrostatic potential on grid points, i.e., by summing the individual Gaussian charge density potentials. In Figs. 4(a) and 4(b), we provide snapshots of the electrostatic potential at two points during the fracture simulation. Initially, the system has zero potential (light shading). As a crack evolves, we observe the production of negative charge carriers in the free space inside the crack. Figure 4(b) shows the final state of the system after the crack has propagated through the unit cell, with the crack edges outlined in black. Heterolytic bond cleavage due to thermal fluctuation and
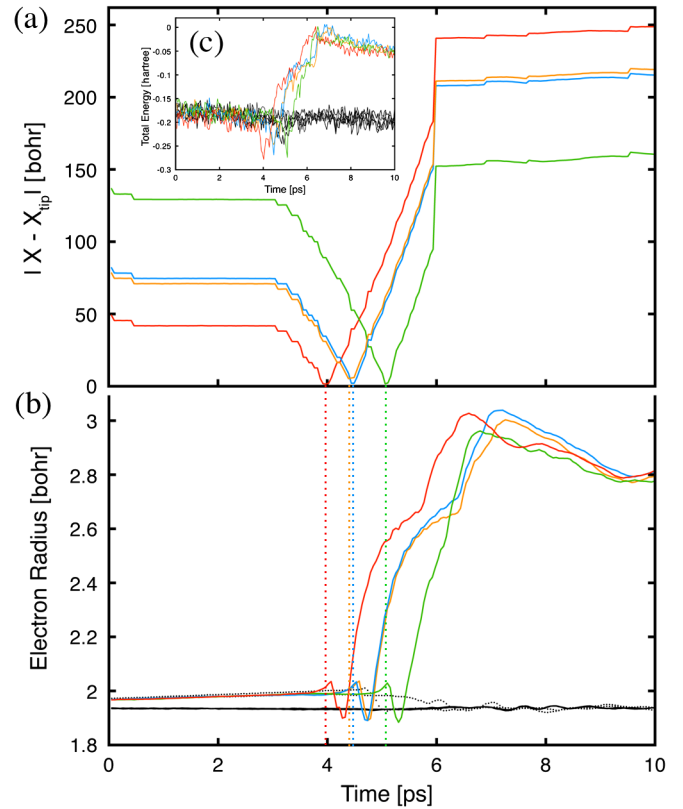

FIG. 3 (color online).   (a) The absolute distance between the crack tip and electrons that will ionize. (b) The radii of ionized electrons (shaded), ground state surface electrons (black dotted lines), and bulk electrons (solid black lines). (c) The total energy of the electrons.

hot spot formation causes $2.6 \times 10^{-2} \pm 1.3 \times 10^{-2}$ more electrons per nm^2 to remain on one side of the crack than the other, which results in the left crack face having ($+$2.13 V) potential and the right face having ($+1.12$ V) potential. The potential gradient across the crack corresponds to a voltage of 1.02 V. Li and colleagues reported measuring voltages of tens of mV with some cracks producing voltages up to 0.39 V [12]. The electrostatic potential difference between the crack surfaces reflects the dynamics of charge carriers during silicon fracture.

We computed the number of ionized electrons at each time point in our crack trajectories (see the Supplemental Material for details and a plot [22]). Given the size of our {111} cell, these correspond to a total electron yield of 5.3×10^{11} to 1.6×10^{12} cm^{-2}. Langford and co-workers detected current transients whose integrated area corresponded to yields of 10^9 or 10^{11} carriers/cm^2, though their {111} crack velocities were around 900 m/s [13]. They stated that faster cracks produced larger carrier yields. Our {111} crack velocity is 2 times faster, which explains why we observe larger ionized electron yields.

From the equilibrium dynamics of the cracked system, we determined the electrical conductivity using the Green-Kubo integral of the electric current correlation function as
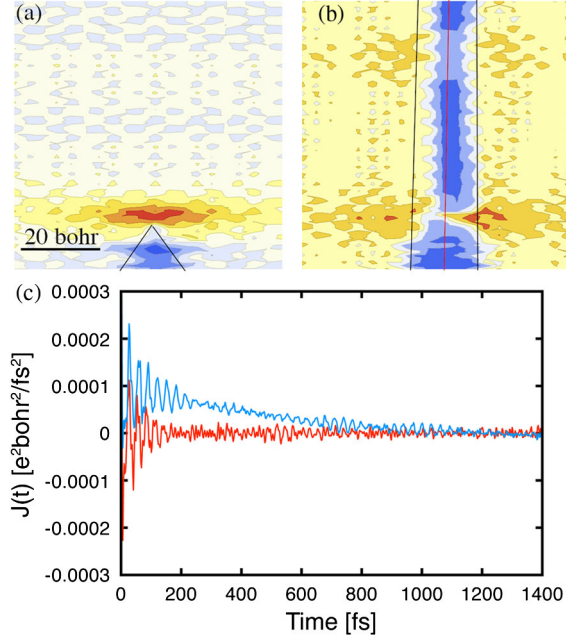
FIG. 4 (color online).   The evolution of electrostatic potential is given at (a) 0 ps and (b) 15 ps. After fracture negative potential is distributed asymmetrically between the crack faces (solid black lines). (c) The electric current velocity correlation functions for the {111} system at equilibrium (lower curve) and after the crack has occurred (upper curve).

$$\sigma_{GK} = \frac{1}{3k_B TV} \int_0^\infty \langle \mathbf{j}(t) \cdot \mathbf{j}(0) \rangle dt, \qquad (1)$$

where $\mathbf{j}(t)$ is the electric current flux, and the integral argument corresponds to the electric current velocity correlation that is expressed as

$$J(t) = \langle \mathbf{j}(t) \cdot \mathbf{j}(0) \rangle = \sum_{i=1}^N \sum_{j=1}^N \langle q_i q_j \mathbf{v}_i(t) \cdot \mathbf{v}_j(0) \rangle, \qquad (2)$$

where i and j are different particles. Figure 4(c) shows the current velocity correlation, $J(t)$, for our {111} system at 300 K and after the crack has occurred. The postcrack data trace is initially positive because free charge carriers are moving across the gap; these carriers have strong autocorrelation signals. Integrating these traces and applying the result to (1) gives us a measure of the conductivity of our cells before and after fracture. Before the fracture our cell has an electrical conductivity of 2.69×10^{-5} S/cm; after fracture the cell has a conductivity of 3.72×10^{-3} S/cm. Pure silicon samples (like our simulation cells) have conductivity as low as 10^{-4} S/cm and decreasing the dopant concentration causes silicon to asymptotically approach 10^{-5} S/cm [30]. Our post crack sample has a calculated conductivity on the order of n-doped silicon samples with dopant concentrations of 4×10^{12} cm^{-3}. This indicates that the production of mobile charge carriers as a direct result of fracture accounts for the experimentally observed

fracture current bursts. It also corroborates the observation of conduction band electrons in Fig. 3(c).

We show here that our effective core potential (ECP) for silicon in the electron force field method provides an accurate representation of the dynamics of material failure, including charge transfer, voltage impulses, and electron ionization. In this study we demonstrated that eFF could replicate the physics of brittle fracture of silicon independent of crack orientation. The equilibrium and dynamic mechanical properties computed from our simulations are in excellent agreement with experimental measurements and the predictions of other reactive force fields. Furthermore, we observed the generation of voltages and the production of charge carriers in good agreement with experiment. We have performed preliminary tests to infer spectral emissions from the ground state and excited electron eigenstates from eFF dynamics, albeit within the limitations of the Gaussian basis set representation and the ECP approximation, by computing the autocorrelation function of the electron wave packets and Fourier transforming this function to obtain the eigenstates of the system. This technique allows us to roughly estimate the emissions that accompany shock, fracture, or triboluminescence.

The significance of these results stems from the capability of eFF to accurately track the long-term dynamics of electrons under nonadiabatic conditions. This provides new insights into the phenomenon of electron ejection, voltage fluctuations, and charge carrier induction. Since eFF has been demonstrated to predict the transformation of H_2 and Li from ground state to intermediate states of warm-dense matter to highly excited and plasma state regimes and Auger decay, we consider that eFF is suitable for treating electronic effects in materials under a wide range of extreme conditions.

*ajaramil@caltech.edu
†wag@wag.caltech.edu

[1] T. Shiota and K. Yasuda, Mater. Sci. Eng. B **173**, 248 (2010).
[2] K. Yasuda et al., Philos. Mag. A **82**, 3251 (2002).
[3] F. Urakaev, Phys. Chem. Miner. **35**, 231 (2008).
[4] J. T. Dickinson, E. E. Donaldson, and M. K. Park, J. Mater. Sci. **16**, 2897 (1981).
[5] J. A. Hauch et al., Phys. Rev. Lett. **82**, 3823 (1999).
[6] D. Holland and M. Marder, Phys. Rev. Lett. **80**, 746 (1998).
[7] F. F. Abraham et al., Europhys. Lett. **44**, 783 (1998).

[8] J. G. Swadener, M. I. Baskes, and M. Nastasi, Phys. Rev. Lett. **89**, 085503 (2002).

[9] M. J. Buehler, A. C. T. van Duin, and W. A. Goddard, Phys. Rev. Lett. **96**, 095505 (2006).

[10] M. J. Buehler *et al.*, Phys. Rev. Lett. **99**, 165502 (2007).

[11] D. Sen *et al.*, Phys. Rev. Lett. **104**, 235502 (2010).

[12] D. G. Li *et al.*, Phys. Rev. Lett. **73**, 1170 (1994).

[13] S. C. Langford, D. L. Doering, and J. T. Dickinson, Phys. Rev. Lett. **59**, 2795 (1987).

[14] C. J. Kaalund and D. Haneman, Phys. Rev. Lett. **80**, 3642 (1998).

[15] E. Busch *et al.*, Appl. Phys. Lett. **73**, 484 (1998).

[16] A. Frost, J. Chem. Phys. **47**, 3707 (1967).

[17] C. Wilson and W. Goddard, Chem. Phys. Lett. **5**, 45 (1970).

[18] J. Su, Ph.D. thesis, California Institute of Technology, 2007.

[19] J. T. Su and W. A. Goddard, III, J. Chem. Phys. **131**, 244501 (2009).

[20] A. Jaramillo-Botero *et al.*, J. Comput. Chem. **32**, 497 (2011).

[21] J. T. Su and W. A. Goddard, III, Phys. Rev. Lett. **99**, 185003 (2007).

[22] See Supplemental Material at http://link.aps.org/supplemental/10.1103/PhysRevLett.108.045501 for a detailed explanation of the eFF method, additional electron dynamics data, ionization yields, stress energy release rate calculation details, and validation of the effective core potential. Animated trajectories can be found at http://www.its.caltech.edu/~ptheofan.

[23] M. T. Kim, Thin Solid Films **283**, 12 (1996).

[24] G. T. A. Kovacs, *Micromachined Transducers Sourcebook* (McGraw-Hill, Boston, 1998).

[25] A. M. Fitzgerald *et al.*, J. Mater. Res. **17**, 683 (2002).

[26] A. M. Fitzgerald *et al.*, Sens. Actuators A, Phys. **83**, 194 (2000).

[27] B. Bhushan *et al.*, J. Mater. Res. **12**, 54 (1997).

[28] F. Ericson *et al.*, Mater. Sci. Eng. A **105–106**, 131 (1988).

[29] J. R. Kermode *et al.*, Nature (London) **455**, 1224 (2008).

[30] R. Hull, *Properties of Crystalline Silicon* (Institute of Electrical Engineers, Herts, England, 1999), pp. 413–414.

[31] N. Bernstein and D. W. Hess, Phys. Rev. Lett. **91**, 025501 (2003).